Analysis of the multi-cracking mechanism of brittle thin films on elastic-plastic substrates

I. Ben Cheikh, G. Parry, D. Dalmas, R. Estevez, J. Marthelot

Version of Record: https://www.sciencedirect.com/science/article/pii/S0020768319303464
Manuscript_d7dfcb261d67308ec75e50dbafc403e7

Analysis of the multi-cracking mechanism of brittle thin films on elastic-plastic substrates

I.BenCheikh[1,2], *G.Parry*[1], *D.Dalmas*[2], *R.Estevez*[2], *J.Marthelot*[3,4]

[1] *Univ. Grenoble Alpes, CNRS, Grenoble INP, SIMAP, F-38000 Grenoble, France*
[2] *LTDS, CNRS, Ecole Centrale de Lyon, 69134 Ecully, France.*
[3] *SVI, CNRS, Saint-Gobain, 93303 Aubervilliers, France.*
[4] *Aix-Marseille Univ, CNRS, IUSTI, 13013 Marseille, France.*

Abstract

Thin brittle films on compliant substrates are used in many applications, as soft electronics and solar cells. When submitted to large tensile strains, those systems undergo multi-cracking. A saturation of the cracks pattern is observed, i.e. no new crack is formed above a given nominal applied strain. Moreover, a characteristic distance between the cracks is observed at saturation. A mechanical analysis is carried out in this paper in order to quantitatively predict the saturation phenomenon. Fracture in the brittle layer, delamination at the interface and plasticity in the substrate are taken into account. The results of finite elements simulations show that both the plastic deformation pattern inside the substrate and the strength of the brittle layer are key elements for predicting the cracks pattern at saturation.

Keywords: Multi-cracking, Elasto-plasticity, Thin films, Compliant substrate, Finite elements modeling, cohesive zone modeling

List of notations

E_f, ν_f	Young's modulus and Poisson's ratio of the layer
E_s, ν_s	Young's modulus and Poisson's ratio of the substrate
h_f, h_s	Layer and substrate thicknesses (respectively)
$\overrightarrow{T}$, $\overrightarrow{\delta}$	Traction vector and opening vector in cohesive zone description
(T_n, T_t)	Normal and tangential components of $\overrightarrow{T}$
(T_n^{max}, T_t^{max})	Maximum normal and tangential components allowed for $\overrightarrow{T}$
G_c	Separation energy (per unit area)
(T_n^i, T_t^i)	Normal and tangential components of $\overrightarrow{T}$ actually reached at peak traction
T_{max}	Strength of the oxide layer, chosen so that $T_n^{max} = T_t^{max} = T_{max}$
δ^i	Magnitude of separation at fracture initiation
δ^f	Magnitude of separation reached at complete separation
H	Size of the layer fragments
L	Size of the Finite Elements calculation cell

Introduction

Thin films are commonly deposited on soft substrates in a large range of technological applications to modify surface properties (*e.g.* optical index, electric conductivity, chemical insulation, wear resistance) [1, 2]. Fracture propagation is however an important limitation, especially in the case of deformable devices. For instance, stretchable electronics technology critically rely on the toughness of electronic circuits embedded in a soft matrix [3, 4, 5, 6]. Such thin films either experience compressive or tensile stresses as the substrate is deformed. Compression may induce the formation of wrinkles [7, 8, 9] and eventually of delamination blisters [10, 11, 12, 13]. Conversely, tensile stresses generally lead to the fragmentation of the coating across its thickness. The condition of propagation of a channel crack in the thin film has therefore been extensively studied in brittle [14, 15, 16, 17, 18] or ductile [19] thin layers.

In the case of thin films supported by elastomeric substrates, essentially undergoing elastic deformations, the cracks can channel through both the film and the substrate at relatively great depth [17, 20]. However, in many applications, thin films are rather deposited on polymeric substrate that presents an elasto-plastic response. Here, we focus on films supported by elastic-plastic substrate, for which the fragmentation process at large deformation involving strain localization in the substrate is still poorly understood. We

explore experimentally and numerically the fragmentation process of brittle coatings deposited on a polymeric substrate. Experimentally, we observe a saturation process of the crack distribution at large strain and a distribution of crack opening that are not captured by perfectly elastic model or simple shear-lag models [21, 22, 15, 23]. We rationalize those two features using finite elements simulation with mixed-mode cohesive zone model, to characterize the plastic strain distribution and the extension of the plastic deformations into the substrate. A first model involving large computational cells with randomly distributed tensile strength values allows to reproduce the various stages of multi-cracking that are also observed experimentally, up to saturation. A second model, based on periodic unit cells and with uniform material properties, is used to study specifically the saturation regime. This model leads to the same predictions of distance between cracks at saturation as the first model, but allows a thorough parametric study because of its much higher computational efficiency. This demonstrates that it is not necessary to simulate the initial defect distribution (i.e. random tensile strength distribution) to study the saturation stage. A comparison of our results is made with predictions of models based on the shear lag hypothesis [21, 24]. The differences obtained show that the mechanism displayed by our calculations, characterized by heterogeneities of deformations inside the substrate, has an influence on the distance between cracks at saturation.

1. Experimental Fragmentation of the brittle layer

Nanometric layers of zinc oxide (ZnO) of thickness h_f ranging from 30 nm to 100 nm (Young modulus $E_f \sim 100$GPa, Poisson ratio $\nu_f \sim 0.35$) were deposited through magnetron sputtering on flexible sheets of ethylene tetrafluoroethylene (ETFE) of thickness $h_s = 125$ μm. Coatings were performed on a roll-to-roll demonstrator (Coflex 600) at the Fraunhofer Institut fur Elektronenstrahl und plasmatechnik (FEP Dresden). Such brittle layers deposited on flexible substrate are prone to fragment under tensile loads [15, 25, 26, 27].

1.1. Substrate mechanical properties

The mechanical behavior of the raw ETFE substrate was determined with a force-displacement machine (Instron) for different strain rates ranging from $0.25\%/s$ to $25\%/s$ on rectangular bands of 50 mm$\times$5 mm. Because the influence of strain rate is very low, Fig. 1 shows the evolution of nominal stress σ_n for an increasing nominal strain ϵ_n for a single strain rate of $0.25\%/s$. For

small deformation ($\epsilon < 2.1\%$), the material displays an elastic behavior with a Young modulus $E_s = 1 \pm 0.05$ GPa below a yield strain $\epsilon_Y = 2.1 \pm 0.1\%$. For intermediate deformations (2.1 % to 20 %), plasticity initiates in the substrate with a hardening response. For large deformations (larger than 20 %), further strain takes place at an approximately constant tensile stress followed by progressive hardening leading to a final tensile stress of $50MPa$ at rupture.

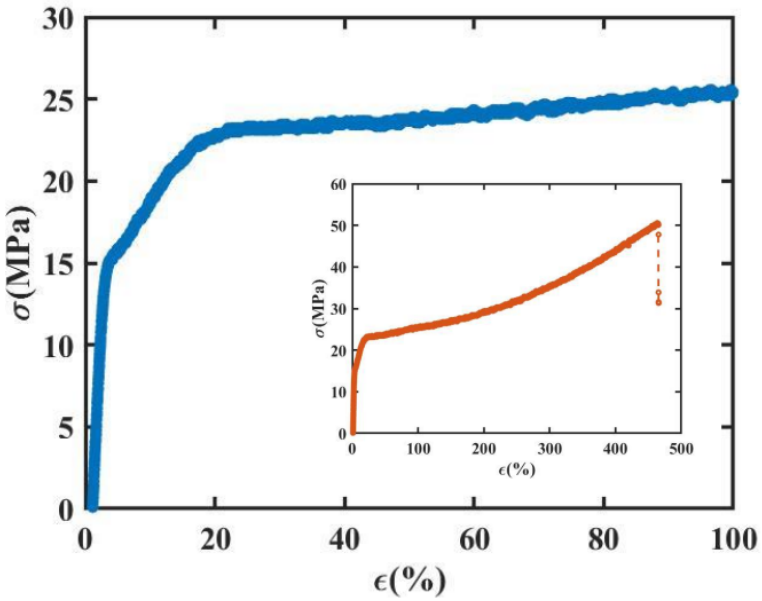

FIGURE 1: Uniaxial tensile test data for ETFE.

1.2. Fragmentation of oxide monolayers

To study the fragmentation process, rectangular specimens of dimensions 50 mm×5 mm were cut from the different samples and submitted to an uniaxial traction in a micro-test tensile stage (Deben) with a strain rate of order 0.1%/s. This low value for the strain rate was chosen to facilitate observations of the fragmentation process. The fragmentation was imaged in situ in the center of the sample by optical microscopy (Fig. 2 (a)), while the strain ϵ was measured independently by monitoring the evolution of the distance between

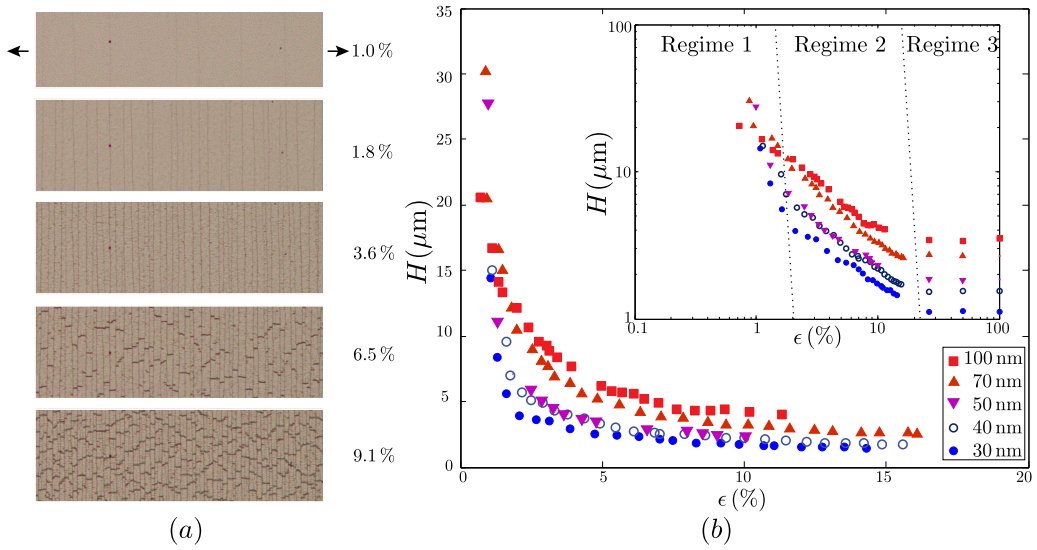

FIGURE 2: (a) Optical microscope images of the cracks pattern at various levels of nominal uniaxial tensile strain (from 1% to 9.1%) for a 50 nm thick monolayer of ZnO deposited by magnetron sputtering on a ETFE substrate. Beyond a critical strain ϵ_c of order 1% cracks successively appear along the width of the sample perpendicular to the stretching direction. As the density of fragments saturates for high strains, delamination blisters appear in the transverse direction beyond a strain of $\sim 4\%$.(b) Mean fragment length H versus applied nominal strain ϵ observed during tensile test of ZnO/ETFE samples. Three regimes can be observed : regime 1 with random initiations of cracks, regime 2 where new cracks appear in the middle of two existing cracks and regime 3 a saturation regime where no new crack is observed.

two stripes painted on the sample. Additional observations were conducted through field emission gun scanning electron microscopy (SEM-FEG) and atomic force microscopy (AFM).

Fig. 2 shows a sequence of microscope images for a representative tensile test performed on a 50 nm thick monolayer. Those images shows that the fragmentation is sequential and that the density of cracks increases with the applied strain ϵ. At higher strains ($\epsilon \sim 4\,\%$), the transverse contraction due to Poisson effect induces the formation of delamination buckles. This secondary buckling is reminiscent of recent investigations on the delamination of thin films adhering on soft substrates [8, 12].

For all the studied specimens, i.e. for the different thicknesses of ZnO layers, formation of cracks is observed above a critical strain ($\epsilon \sim 1\%$). The cracks propagate perpendicularly to the direction of traction and post-mortem observation of the samples by SEM-FEG indicates they propagate all along the thickness of the layer ('channel crack') and do not penetrate into the substrate, neither branch at the interface. The fragmentation is thus unidimensional and can be characterized by the length of the fragments H defined as the distance in the stretching direction between two successive transverse cracks. For large deformation ($\epsilon > 20\%$)), we observe that the fragmentation process stops leading to the saturation of the distance between cracks. The mean fragments size H has been measured as a function of the applied strain (Fig. 2 (b)). H, which is averaged on a large number of cracks (about hundred) for the different thicknesses of ZnO layers, decreases progressively with ϵ and eventually saturates at large strains ($\epsilon > 20$ %) as the fragmentation process stops. As a general trend, thicker layers also lead to larger fragments, for a given strain level.

Based on optical observations and on the evolution of H versus ϵ, we were able to define three successive regimes :

- The first one ($\epsilon < 2\%$), during which there is no clear dependence to the deformation, corresponds to a statistical regime with no obvious spatial organization. Each new crack appears at random position mainly driven by the presence of defects in the layer.
- The second one ($\epsilon \in [2-20]\%$) correspond to a sequential stage during which each new crack appear in the middle of previous fragment (mid-island breaking). This stage is described theoretically by [23].
- The last one is a saturation regime during which no new cracks appears.

It is worth noting that similar log-log representations of inter-cracks distances versus applied strains can be found in [28, 16]. In those references, the authors have been able to identify only two stages, which is probably due to the particular nature of their substrate (polyimide).Different mechanisms have been proposed to explain the saturation of the width of the fragments in other experimental systems. The penetration of the cracks into the substrate [17] or a delamination between the film and the substrate [29, 30, 31, 27, 15, 25] may for instance been involved. However, local observations with SEM-FEG in our case do not evidence any signature of such processes. In our opinion, as suggested by the stress-strain curve for ETFE, the plastic deformation of the substrate should nevertheless constitute a re-

levant candidate to account for the observed saturation. In the next section, we propose experimental evidences showing how the plastic deformation in the substrate is coupled with the development of cracks in the film, with plastic strains localization in the fracture grooves.

1.3. Localization of the deformation in the substrate

The first experimental evidence of the localization of the deformation in the substrate is obtained by observing a sample after acid etching of the fragmented layer. By dipping a part of the sample into beaker filled with hydrochloric acid during a few minutes, it is possible to locally remove the ZnO layer without damaging the substrate. On Figure 3(a), which shows an optical image of the sample after this acid etching, we observe that groove are still visible on the naked substrate (right side) even if the layer is removed. By performing AFM images on the naked side of the sample (figure 3(b)), an horizontal groove perpendicular to the loading direction has been observed confirming that the substrate is irreversibly deformed due to plastic deformation. This deformation is localized in the crack opening region, the polymer being otherwise protected by the rigid layer. On figure 3(b), one can notice that buckling also induced permanent plastic deformation since two folds, that could correspond to both fronts of the buckle, are still visible on the bottom of the image.

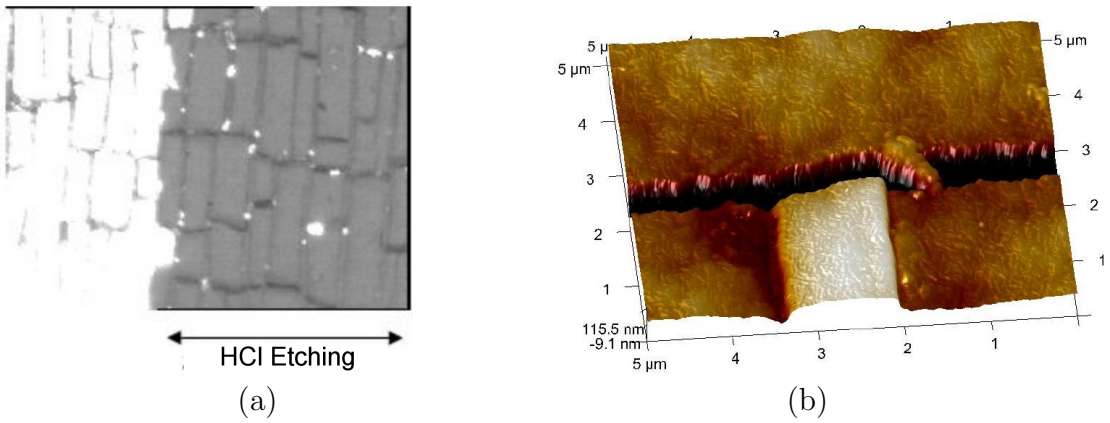

(a) (b)

FIGURE 3: Optical (a) and AFM (b) images of the substrate surface after chemical coating removal, showing evidence of a strong localized plastic deformation of the substrate in the crack area.

To confirm the presence of localized plastic deformation in the substrate, we performed AFM images of the samples under loading at different strain (cf. Fig 4) for a monolayer of oxide of 100 nm. On Figure 4(a), contrary to what is predicted by purely elastic models [32, 23, 1] (i.e. an uniform distribution of crack opening), we observe that the distribution of crack opening is very large at a given strain. Indeed, the cracks which appear at small strain are more open than the cracks which appear later (cf. Fig 4(b)). For example, the channel crack labeled (1) that initiates at a strain of approximately 1% has an opening of about 400nm at a strain of 5.1 % whereas the channel crack labeled (4) has an openig of less than 100nm at the same 5.1% strain. We measured by AFM the evolution of the opening during the loading for four different cracks (cf. Fig 4(c)) and show that their opening depend on their history (i.e. the strain at which they were nucleated). The opening of each crack increases linearly with the imposed macroscopic deformation so that we can estimate the history of propagation and the critical strain at nucleation for each crack from the measurement of their opening on a single image.

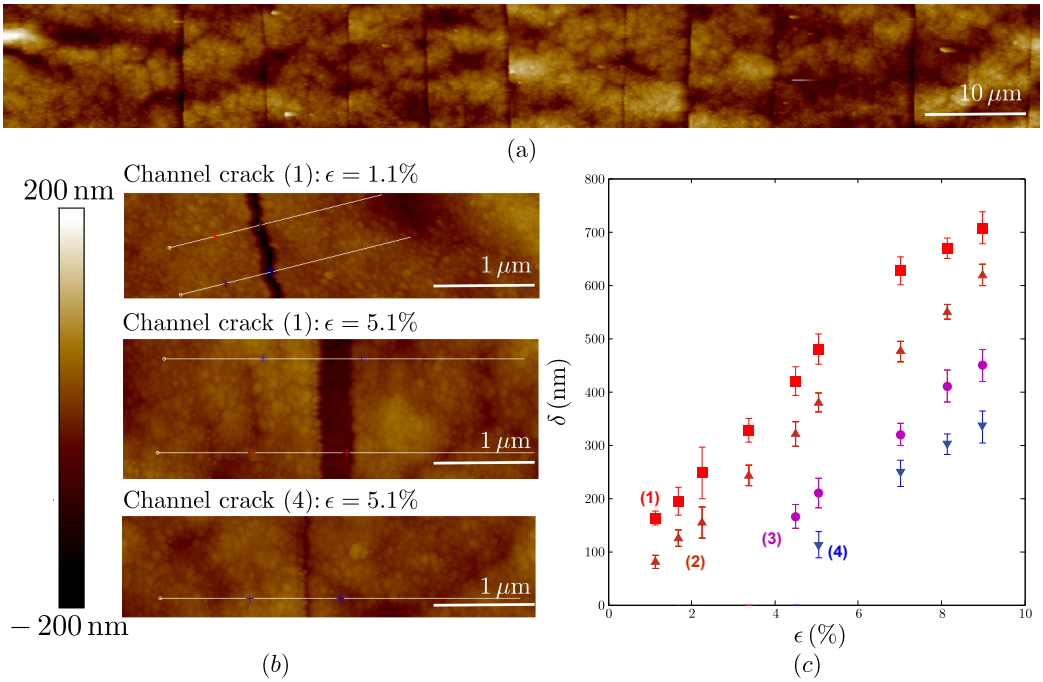

FIGURE 4: (a et b) AFM images at different scales of the surface of a 100nm oxide layer under tensile loading. The crack opening is clearly not uniform. A crack which appears at small strain is more opened than a crack which appears later. (c) Evolution of the crack opening as a function of the nominal stain for four different cracks.

2. Model description

2.1. Geometry, materials and boundary conditions

To further study and understand the multi-cracking phenomenon of brittle thin films on compliant substrate, a 2D plane strain model was developed. In this model, a linear elastic isotropic layer of $100nm$ in thickness with Young's modulus E_f=100 GPa and Poisson's ratio ν_f=0.35 is considered, in accordance with experimental data. The layer is brittle. The soft substrate (ETFE) is considered elastic-plastic, with a linear elastic behavior (Young's modulus E_s=1 GPa and Poisson's ratio ν_s=0.45) and an isotropic hardening. The stress vs strain relationship for the substrate is shown in Fig 1-(b). This law is based on experimental data resulting from the experiments described in section 1.1.

To model cracks formation and interface debonding, a mixed-mode cohesive zone (CZM) model is used. CZM are widely used in computational

fracture mechanics due to their easy implementation in FEM codes, simple formulation, and flexible applications in interface modeling and crack growth analysis [33, 34]. The constitutive behavior of the CZM consists of a traction versus separation law. Due to interaction between the two separating faces, the interface traction vector $\overrightarrow{T}$ depends upon the separation vector $\overrightarrow{\delta}$, which is the relative displacement between opposite crack faces at a point initially joined on the interface (see Appendix for details).

In this general framework, only three independents parameters are generally necessary to describe the cohesive zone behavior : T_n^{max}, T_t^{max} and G_c (or alternatively δ^f). Furthermore, our choice is to consider that any opening prior to interface damage has no physical meaning, so we set the numerical parameter K large enough so that $\delta^i << \delta^f$.

Note that in the case of a brittle oxide layer, where all the cracks appear in opening mode, the relevant parameters can be reduced to two, that are chosen as T_n^{max} and δ^f. However in the case of an interface, for which loading consists of a mixture of shear and normal tractions, three parameters are required.

As our work hypothesis (based on the aforementioned experimental observations) is that plasticity governs the final crack pattern at saturation, the interfacial characteristics has been chosen in such a way that only a small area of the interface is delaminated when an oxide crack reaches the interface. Thus in our calculations, the maximum interfacial delamination length is of the order of the layer thickness, whereas the stress relaxation inside the layer due to the formation of a plastic area along the interface will be much larger.

To model a tensile test on our simulation cells (see description below and Fig. 5), the displacement in direction x is blocked on their left side ($U_x(O, y) = 0, \ \forall y$) and set at U on their right side ($U_x(L, y) = U, \ \forall y$) so that the nominal strain applied to the simulation cell is $\bar{\epsilon} = \frac{U}{L}$ (with L is the cell's length). U is progressively increased from 0 to a maximum value U_{max}. Periodic boundary conditions are applied to the vertical edges of the calculation cell so that all the points on the edges have the same displacement in the y-direction, i.e : $U_y(0, y) = U_y(L, y), \ \forall y$.

One quantity of interest that will be used in the analysis is the mean stress inside the layer in the traction direction, which is defined as :

$$\bar{\sigma}(x) = \frac{1}{h}\int_0^h \sigma_{xx}(x,y)dy \tag{1}$$

h is the thickness of the layer, and x, y are the coordinates of a point inside the layer.

The Finite element implementation of this model was carried out using the commercial finite element code ABAQUS [35]. Plane strain triangular and quadrangular elements, with quadratic interpolation were used in both layer and substrate. The CZM model was implemented using the standard element COH of the ABAQUS elements library. Finally, an implicit integrations scheme was used (ABAQUS standard solver).

2.2. Large cell model

To simulate the multi-cracking phenomenon and more specifically to reproduce the three stages of multi-cracking observed experimentally and described in section 1.2, simulations have been carried out on large 2D cells, with a large number of potential positions for cracks in the layer, as shown in Fig. 6. This is done by introducing CZ elements in between each neighboring standard 2D quadrangular elements of the layer, along the vertical directions (see red lines in Fig.6). For example, in a 30 μm wide cell, about 750 CZ elements (i.e. potential crack nucleation sites) are introduced. As will be seen further, only a much smaller number of cracks (of the order of 10) are propagating through the layer in this case (Fig 7-(e and f)). This choice allows minimizing the influence of the mesh on the final cracks position. The CZ elements inserted obey to the linear/softening relation described in Appendix. As discussed previously, only the normal traction is involved in the crack nucleation and propagation criterion for the layer. So we will denote in the following T_n^{max} as T_{max}. T_t^{max}, that has been chosen equal to T_n^{max} in the layer for the calculations, will hence not been mentioned further in the text.

To avoid a simultaneous opening of the cohesive elements implemented in the layer which will naturally occurs if all the CZ are identical, a random distribution of T_{max} has been used :

$$T_{k,max} = T_{max} + \Delta T_{k,max} \tag{2}$$

where $T_{k,max}$ is the normal cohesive strength of the k-th CZ element and $\Delta T_{k,max}$ represent a noise which ensures an non homogeneous distribution

of T_{max} for all CZ elements . $\Delta T_{k,max}$ have been chosen so that $T_{k,max}$ follows a Gaussian distribution (Fig 6, inset) with a mean value T_{max} with a standard deviation ΔT_{max}. The introduction of distributed value of $T_{k,max}$ in the layer is assumed to be more realistic as it will account for the strength heterogeneity in the layer due to defects like microstructural heterogeneities or pores. Thus, those large cell simulations are providing a way to compute the distance between cracks at saturation as a function of the layer mean strength T_{max}.In addition, the fact already mentioned that less than 1% of the CZs introduced into the simulation evolves into cracks prevents any further analysis of the influence of the chosen distribution because only the few extreme values matter. For the sake of simplicity, we have chosen a Gaussian distribution but some simulations not presented here with other types of distribution (e.g. uniform, Weibull) have led to the same results and analyzes.

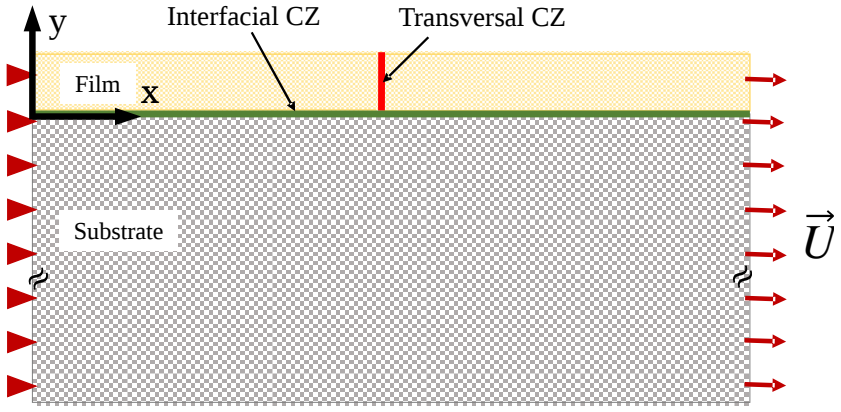

FIGURE 5: Schematic representation of the unit cell model

2.3. Unit cell model

As the large cell model previously presented will naturally request a high calculation time and a lot of data storage, we also carried out simulations on smaller unit cells of various length with only one potential crack in their middle (Fig. 5). Due the periodic boundary conditions of our simulation, they will allow the simulation of a periodically cracked layer. Indeed, if we want to focus on the second cracking stage and the subsequent crack pattern

saturation (Fig. 2 (b)), it can be assumed that the crack spacing is equal at a given loading state. It is then possible to reduce the problem to a unit cell that contain only one transverse crack in the middle which is simulated by the introduction a cohesive zone in the center of the cell, with periodic boundary conditions along the vertical edges.

The results from this unit cell model will be compared to the predictions of the large cell model.

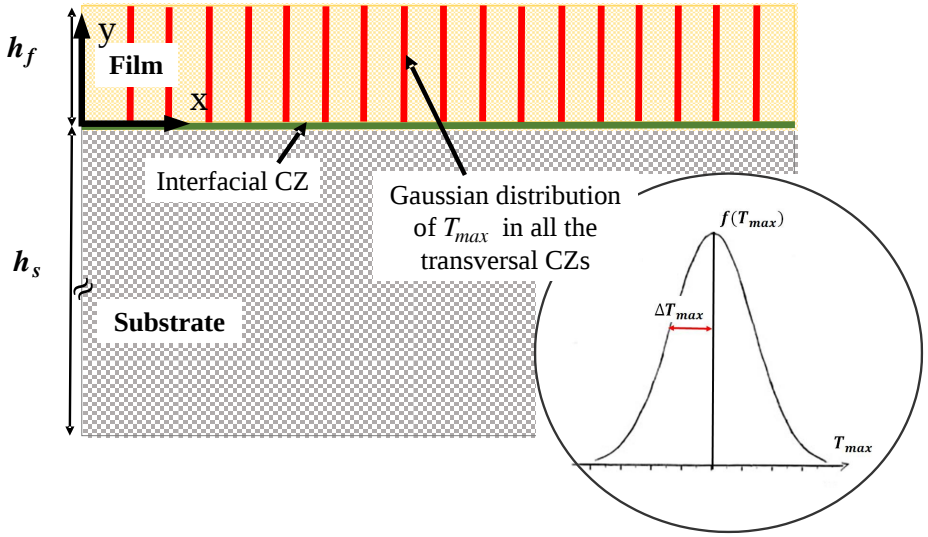

FIGURE 6: Large cell including a random (Gaussian) distribution of strength T_{max} inside the layer.

3. Results and discussion

In this section, results of simulations carried out with large cells are first displayed in order to demonstrate the ability of the model to capture the 3 stages of multi-cracking observed experimentally. The effect on the layer strength (i.e T_{max} in the simulation) on the cracks distances at saturation is reported.

Then, stage 2 (mid-island breaking) is studied in more details using the periodic unit cell model. The use of this model, numerically less intensive,

allow for a detailed investigation and understanding of the stress variation inside the layer. In particular, the relationship between the plastic deformation inside the substrate and the evolution of maximum stress reached in between two cracks during loading (σ_{max}) is studied. A saturation distance between cracks is obtained from this model and is compared to the one obtained from the large cell calculations.

3.1. Large cell simulations results

Details for geometry, constitutive parameters, loading and boundary conditions for the large cell simulations are provided in section 2. The CZM parameters, for both the layer and the layer/substrate interface are reported in Table 1 [1].

Some details should be given about the choice of the cohesive parameters for the oxide layer. In the calculations, we have chosen to set the critical opening of the layer oxide to $\delta_c = 4\ nm$, which is of the same order of magnitude as in [36]. Once δ_c is fixed, only one parameter can be varied. In our case, we have chosen to vary T_{max}, in a range that is consistent with experimental data from the literature [15]. The value of G_c is derived from the choice of the pair (T_{max}, δ_c). The set of values chosen here reflects the brittle behavior of the oxide, which fails locally as soon as $\sigma_{xx} = T_{max}$ is reached. In other words, the critical step for layer failure is the initiation step controlled by T_{max} [2].

Parameters	Layer	Interface
G_c (J/m^2)	$0.1 - 0.8$	5
T_{max} (MPa)	$50 - 400$	100

TABLE 1: Cohesive zone parameters used in the FE simulations.

On Fig. 7 which reported the typical results of a large cell simulation, contour plots of the equivalent plastic strain are displayed on the left ((a),(c) and (e)), whereas values of the average stress $\bar{\sigma}$ in the layer are displayed on

1. For the interface, the value T_{max} indicated in the table is such that $T_n^{max} = T_t^{max} = T_{max}$

2. Calculations have also been carried out fixing T_{max} and varying G_c. The influence of G_c on the propagation of the crack through the thickness was shown to be minor. In other terms, in our particular case the T_{max} parameter governs fracture.

the right ((b),(d) and (f)), at various nominal strain levels $\bar{\epsilon}$. Note that only a small part of the big-cell is represented in Fig. 7, for clarity. Nevertheless, all the simulation performed in this study allow to recover the 3 stages observed experimentally :

- Stage 1 where first defects triggered cracks at random locations (Fig. 7a and b). Those first defects corresponds to some of the CZ with the lowest T_{max}, i.e. the extreme values in the gaussian distribution.
- Stage 2 where sequential mid-islands cracking is observed (Fig. 7c and d),
- Stage 3 where no further cracks are observed which corresponds to a saturation regime (Fig. 7e and f).

Cracks that can be identified in Fig. 7a by gaps in the oxide layers (upper layer) are generating a strong stress concentration in the region of the substrate located in the neighborhood of the crack tip. This causes localization of the plastic strain in the substrate just underneath the layer (butterfly wings shape). It is worth noting that the plastic strain is localized in bands located right and left of the crack, tilted from about 45° with respect to the horizontal direction. Note that the formation of such localized areas with a strong plastic deformation is favored by the small hardening of the substrate. In contrast, it reveals a triangular shaped region in between two neighboring cracks where the plastic strain is rather moderate (dark blue). The model thus predicts a strain distribution in the layer that is heterogeneous. It is all the more important that this aspect is not featured in purely elastic models as well as model based on shear lag theory [21, 26]. For increasing values of $\bar{\epsilon}$, the density of cracks tends to increase (Figs. 7-(b) and 7-(c)), but the heterogeneous distribution pattern for plastic strain is conserved, with the same triangular islands of substrate exhibiting moderate strain in between cracks (scaled down compared to Figs. 7-(a)), the plastic strain being localized underneath (red to gray colors). This heterogeneous distribution of the plastic strain in the substrate is in good agreement with the heterogeneous crack opening observed experimentally in Figure 4. In particular, as observed in Fig.7-(c), newly formed crack present a smaller opening than crack that appear at smaller deformation.

The stress distribution $\bar{\sigma}$ inside the layer for various levels of applied nominal strain $\bar{\epsilon}$ is depicted Fig. 7b,d and f. In Fig. 7b, an initial plateau with a slight noise can be observed for $\bar{\epsilon}$ smaller than 1%.

The roughness of the curve is a consequence of the heterogeneous distribution of T_{max} along the layer. The small drops on the curve correspond

to the early stage nucleation of cracks in the layer. At higher applied strain levels, $\bar{\sigma}$ locally drops to zero, corresponding to cracks that have propagated across all the layer thickness.

The first drop to zero (i.e. the fist through-thickness crack) occurs at 1.5% applied strain. At $\bar{\epsilon} = 2.8\%$, several cracks can be observed, all of them arising from the first random cracking stage. At this point, it is interesting to examine the stress profiles in between two neighboring cracks. As expected, $\bar{\sigma}$ vanishes where the through-thickness cracks are located, and reaches a peak at the middle point between two cracks. This can be seen all along the simulation box at $\bar{\epsilon} = 2.8\%$, meaning that the system has entered stage 2 at this point. The stress distribution is peaked enough so that the loci for the next cracks can be clearly identified at these peaks.

Fig. 7d describes the subsequent stage 2 (mid-island cracking). A typical middle crack formation can be observed between $\bar{\epsilon} = 5.8\%$ and 6.2% . The peak stress can be seen to sharply fall down, with a much lower stress obtained over the newly formed islands. This means that a large increase of the applied strain would be necessary to reach T_{max} again in the middle of the fresh islands. But this is not possible because all the plastic strain is now localized way underneath the 'archipelago' of layer islands (Fig. 7e). The origin of the saturation of the multi-cracking patterned is illustrated in Fig. 7f, where one clearly see the 'saturation' of the peak stress that is now very unlikely to reach T_{max} again. Note that at the strain levels displayed in Fig. 7f, the saturation has not been rigorously reached as the peak stress keeps on increasing, but at a very small rate. We will show that a real saturation occurs at larger strain in the next section 3.2.

Similar simulations have been carried out for various values of T_{max}. The distances between the cracks at saturation are extracted from the simulations and reported in Fig. 8 under the shape of an histogram representing the population of cracks versus the inter-crack distances at saturation [3]. The main result is that the mean distance between crack at saturation tend to increase with T_{max}. It can also be observed that the width of distribution of inter-cracks distances tend to get wider as T_{max} increases.

3. Note that the vertical dashed lines refer to results of calculations on periodic unit cells, and will be commented later in the text.

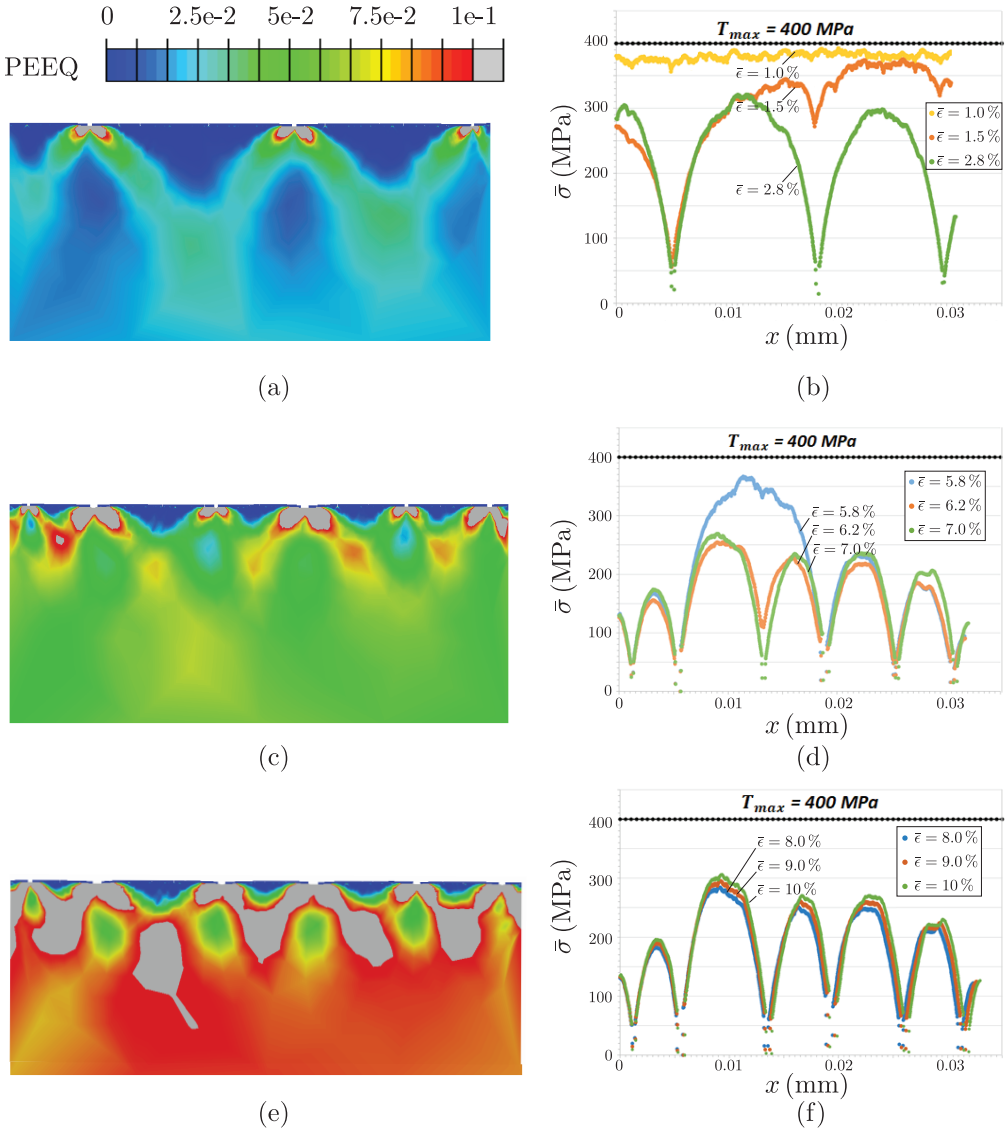

FIGURE 7: Results from large cell calculation. (a),(c),(e) : snapshots (zone of initial length of $30\mu m$) of the plastic strain distribution in the substrate for increasing external strain loading $\bar{\epsilon}$ (nominal strain equal to 2.8%, 7% and 10% respectively, corresponding to the green curves on the right). Location of cracks can be identified from strain concentration. (b),(d),(f) : mean stress $\bar{\sigma}$ variation in the layer versus position x for various levels of nominal strain (indicated at the top right of each figure). Location of cracks can be identified at points where $\bar{\sigma} = 0$. The maximum traction value used in the calculations ($T_{max} = 400$) has also been included.

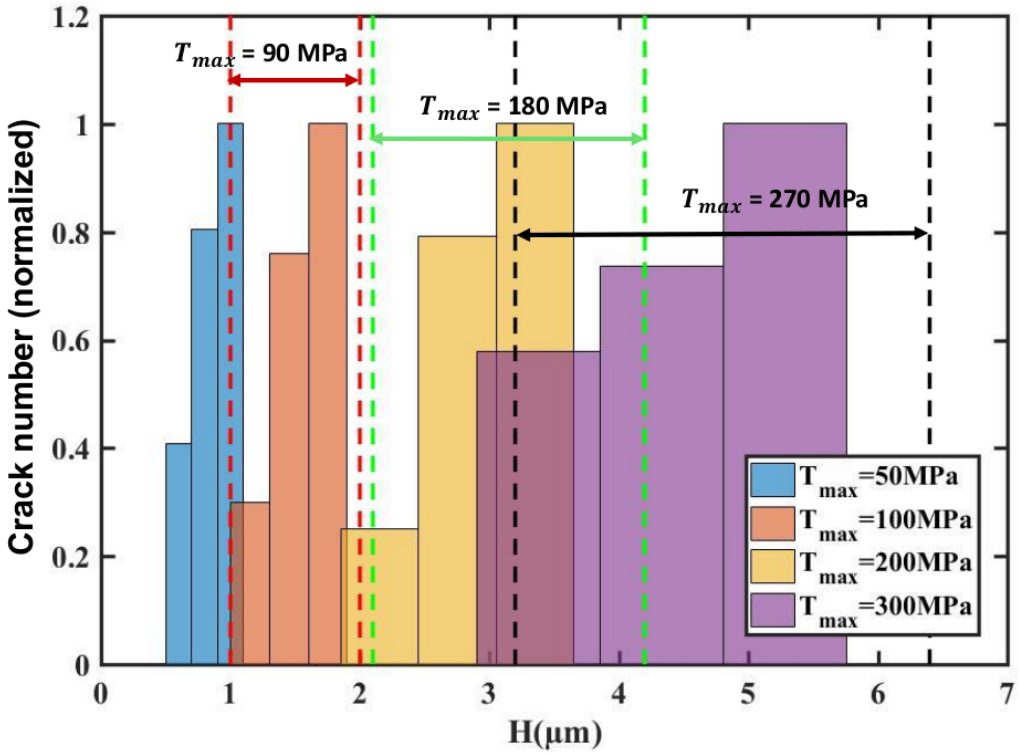

FIGURE 8: Histogram of distances between cracks at saturation (normalized by the most probable distance) H obtained from large-cell calculations for various values of T_{max}. Dashed lines correspond to the theoretical boundaries obtained from the periodic unit cell calculations (see section 3.2).

3.2. Periodic unit cell results

3.2.1. Stress distribution inside the layer

In this part, we will mainly focus on studying the origin of the multi-cracking phenomenon during stage 2 (mid-island breaking) thanks to simulation with periodic unit cells of various length L. Details for geometry, constitutive parameters, loading and boundary conditions for the periodic unit cell simulations are provided in section 2. Note that, due to the periodic boundary conditions of the model, the length L of the cell also represents the distance between two neighboring cracks at initiation. Thus, L can be compared to the experimental size of the fragment H as the crack opening at initiation is negligible.

Fig. 9a presents the typical deformed shape of a layer/substrate unit cell in the neighborhood of a crack. A mapping of the equivalent plastic strain in the substrate is superimposed to the figure. The first point worth noting is the morphology of the layer/substrate around the center crack. Just as suggested by experimental observations (Fig. 3), a groove can be observed underneath the crack. The calculations show that this is due to the emergence a large plastic flow in this neighborhood of the crack. Indeed, the effect of the crack is to create a strong stress concentration inside the substrate, especially a strong shear along the interface, promoting plastic deformation.

The evolution of the mean stress inside the layer $\bar{\sigma}(x)$ as a function of its position along the x axis, calculated from the unit cell simulation, is displayed on Fig. 10a. As expected, it is vanishing at the crack location ($\bar{\sigma}(0) = 0$) and monotonically increases from the center to reach a maximum value, σ_{max} at the edges of the cell ($\bar{\sigma}(L/2) = \bar{\sigma}(-L/2) = \sigma_{max}$). The edges of the cell actually represent the center point between 2 cracks, so it is precisely where the maximum values of $\bar{\sigma}$ is expected. This stress profile is qualitatively consistent with the one assumed for stage 2 in different models found in literature [14, 23]. The value of σ_{max} is naturally a key data since a potential new through-thickness crack will be able to nucleate in the middle of two pre-existing cracks as soon as $\sigma_{max} = T_{max}$.

In addition to those expected results, our simulations allow to shed light on the effects of the presence of an elastic-plastic substrate. Indeed, the evolution of σ_{max} with the nominal (imposed) strain $\bar{\epsilon}$ is no more monotonic, but exhibits 3 remarkable points : one local maximum A, one local minimum

B and one global maximum C as observed in Fig. 10b. Also, computed stress profiles $\bar{\sigma}$ versus position X have been reported for the four applied strains levels corresponding to point A to D in Fig. 10c. It appears clearly that $\bar{\sigma}$ is smaller everywhere in sate D compared to state C.

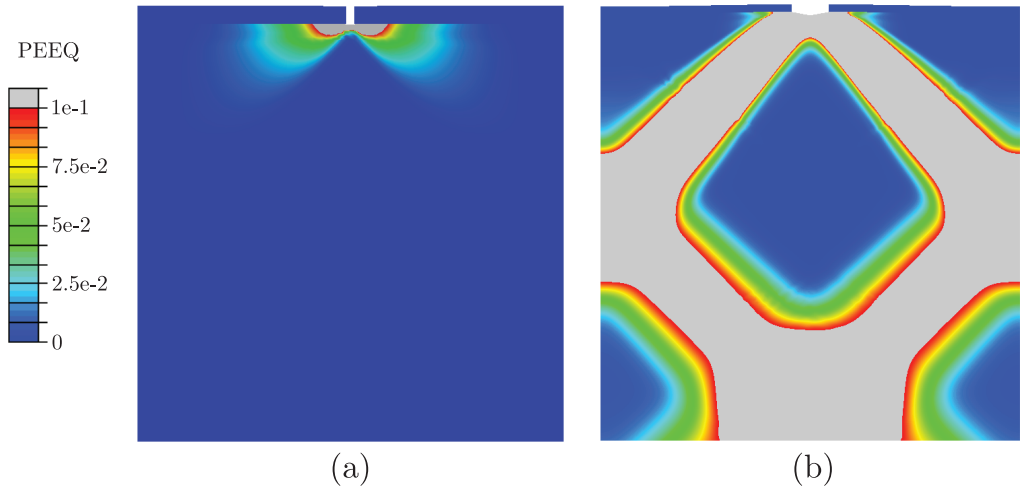

FIGURE 9: Plastic strain distribution inside the substrate during loading. a) an area of plastic deformation is spreading from the crack, along the interface, up to the nominal strain $\bar{\epsilon}$ corresponding to point A (see. Fig. 10). Shear band appear for $\bar{\epsilon}$ between A and B (see. Fig. 10).

The inspection of the deformation in the substrate (Fig. 9) reveals some correlations between plastic deformation patterns and the regime observed in Fig. 10b. During the first loading stage (between points O and A), even if the macroscopic behavior is nearly elastic (linear curves), a plastic zone starts spreading along the interface, taking the shape of butterfly wings (Fig. 9a). The strong shear near the crack edges (see e.g. [37]) is responsible for this local plastic zone. During the transition from A to B, marking a little hook-like drop of the curve, a change in plastic deformation morphology can be observed (Fig. 9b) : shear bands spread from the initial plastic area to reach the edges of the cell. Remembering that periodic boundary conditions are used, this is due to the fact that those bands are meeting the bands emerging from the 'virtual' neighboring cracks (from neighbor cells).

The spreading of plastic deformation along the interface has been further investigated in Fig. 11, where the variation of the extent a of the plastically deformed area versus the applied strain has been reported, for various unit cell lengths L. The results show that plasticity spreads along the interface up to an applied deformation of about 1.2%, after what the plastic zone dimension a remains constant, whatever the cell length L. This strain value of 1.2% marks the threshold between the two aforementioned plasticity regimes : local plasticity due to the stress concentration induced by the geometrical singularity associated to the crack (surface plasticity) and global plasticity in the sample with strain concentration in shear bands (volume plasticity).

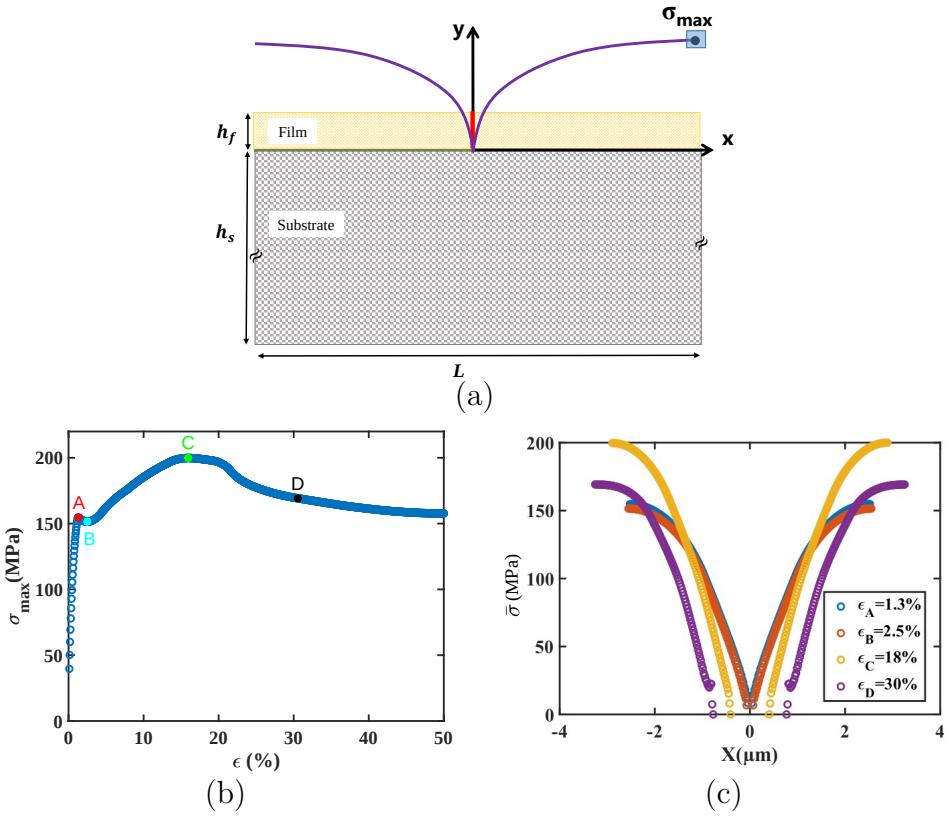

FIGURE 10: Variation of the layer mean stress σ : schematic representation of $\sigma(x)$ along the layer (a). The stress σ vanishes at the crack, while it is maximum ($\sigma = \sigma_{max}$)at the boundary (i.e. right between two neighbor cracks). Four remarkable points reported on the evolution of σ_{max} versus nominal strain loading ϵ (b) and the corresponding stress profiles in the cell (c).

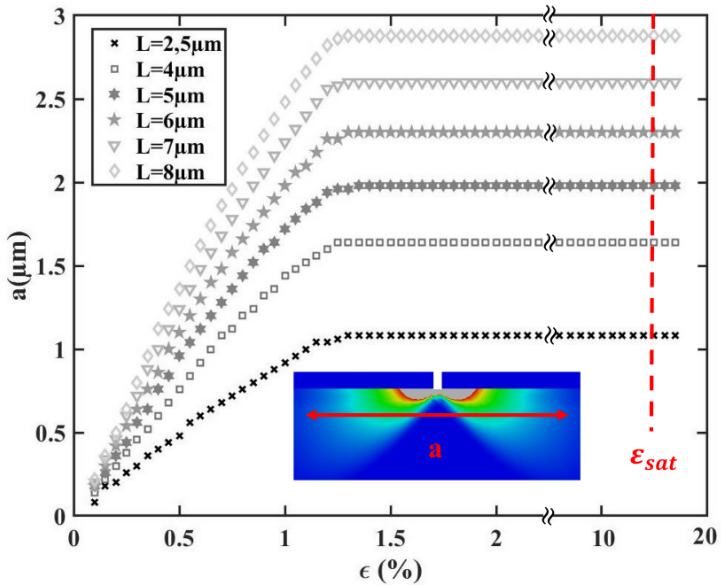

FIGURE 11: Extension of the plastic area in the substrate close to the interface, versus applied strain, for different cell lengths.

Finally, σ_{max} restarts increasing with $\bar{\epsilon}$ (between points B and C) and reaches a maximum at point C before finally decreasing beyond point C. A relationship can be established between those observations and the hardening behavior of the substrate. Indeed, as σ_{max} is increasing, the substrate is nominally in the first hardening regime (see Fig. 1. Likewise, σ_{max} is decreasing while the substrate is nominally in the second hardening regime (Fig. 1.

The most remarkable observation that can be drawn from this simulations results is the existence of a maximum value of σ_{max} (point C in Fig. 10) that cannot be exceeded whatever the value of the applied strain $\bar{\epsilon}$. This clearly indicates that the mid-island fragmentation process (multi-cracking stage 2) has to encounter saturation due to the particular hardening behavior of the substrate. In the example of Fig. 10, with islands measuring $5\mu m$ long, if the strength T_{max} of the layer takes any value above 200 MPa, it will be impossible to have a new crack appearing in the middle of the island, whatever the intensity of the external straining. Note that this saturation phenomenon would not exist in the case of a purely elastic substrate since in

this case σ_{max} would increase proportionally to $\bar{\epsilon}$, whatever the size L of the islands.

3.2.2. Analysis of the crack pattern saturation

Calculations similar to the one reported in Fig. 10 show that the evolution of $\bar{\sigma}$ as a function of ϵ and more particularly the value of the maximum stress σ_{max} depends on the island size L (i.e. the inter-cracks distance). Simulations leading to the results presented in Fig.10 (b) have been repeated for various values of L. They allow to map the evolution of σ_{max} both as function of L and $\bar{\epsilon}$. This mapping, reported Fig. 12a, correspond to the interpolated results of all calculations. It is worth noting that the peak value of σ_{max} is decreasing for decreasing values of L, showing a stronger tendency for saturation as the islands become smaller and smaller.

Our goal in this part is to use the results of the unit cell in order to compute the distance between cracks at saturation for a layer of given strength i.e. of given T_{max}. Curves corresponding to isovalues of σ_{max} when both L and ϵ are varied can be obtained by cutting the surface plot of Fig. 12a by horizontal planes as it is illustrated for $\sigma_{max} = 300MPa$ and $\sigma_{max} = 200MPa$. Now, as an example, assuming that the strength of the layer is $T_{max} = 200MPa$, it is clear that only the area located underneath the $\sigma_{max} = 200MPa$ plane contains equilibrium states, because σ_{max} cannot exceed T_{max}. From here, it is convenient to represent the equilibrium states of the system in the cutting plane itself, as it is done in Fig. 12b. The forbidden area represents the region where no equilibrium state can be found without adding a new crack in the system. Fig.12-b) then allows for the determination of the successive mid-island failures as now explained.

Consider an initial state with cracks distant from L_0 (initial equilibrium point $(L = L_0, \epsilon = 0)$). When increasing ϵ, the loading path follows *an horizontal line* $L = L_0$ up to a value of $\epsilon = \epsilon_1$ such that the green boundary line in Fig. 12b is met. At this stage, $\bar{\sigma} = T_{max}$ and conditions are met to nucleate a new crack in the middle of the island. Thus, the islands length L is divided by 2 ($L = L_0/2$). From this new loading point ($L = L_0/2, \epsilon = \epsilon_1$), the loading path is follows a new horizontal line at $L = L_0/2$ until the boundary curve is reached again and a new fragmentation is possible. Due to the particular shape of the boundary curve that present a minimum, after a number of successive fragmentations, it will necessarily occur that the horizontal loading path will not cross the boundary anymore, since this

boundary has the property of having a minimum in the (ϵ, L) plane : this is defined as the saturation condition.

From this description of the fragmentation process, three stages can be identified :

In the first one, observed for small values of ϵ, the criterion $\sigma_{max} = T_{max}$ is quickly reached and all islands bigger than 6.5 μm are broken. Thus at the end of stage 1, at $\bar{\epsilon}$ close to 1% (point P_1 in Fig. 10b) the biggest distance between cracks should be $L_{max}(P_1) = 6.5\ \mu m$ and the smallest $L_{max}(P_1) = 3.25\ \mu m$.

During stage 2, for $1\% \leq \bar{\epsilon} \leq 18\%$ (between point P_1 and P_2), σ_{max} is globally decreasing with ϵ, but with a much smaller slope compared to stage 1. All the islands with lengths ranging between 6.5 μm and 5 μm fail, giving final islands of lengths ranging between 3.25 μm and 2.5 μm. In the meantime, the islands formed during stage one, with lengths ranging between 5 μm and 3.25 μm survive stage 2. So finally :

all the inter-crack distances belong to the interval $[L_{min}(P_2) = 2.5\ \mu m, L_{max}(P_2) = 5\ \mu m]$, for this particular value of T_{max}.

During stage 3, i.e. beyond point P_2, σ_{max} rises again with $\bar{\epsilon}$, but all the surviving islands have size smaller or equal to $L_{max}(P_2)$, so no loading path can cross the boundary again : this is marking saturation, as mentioned before.

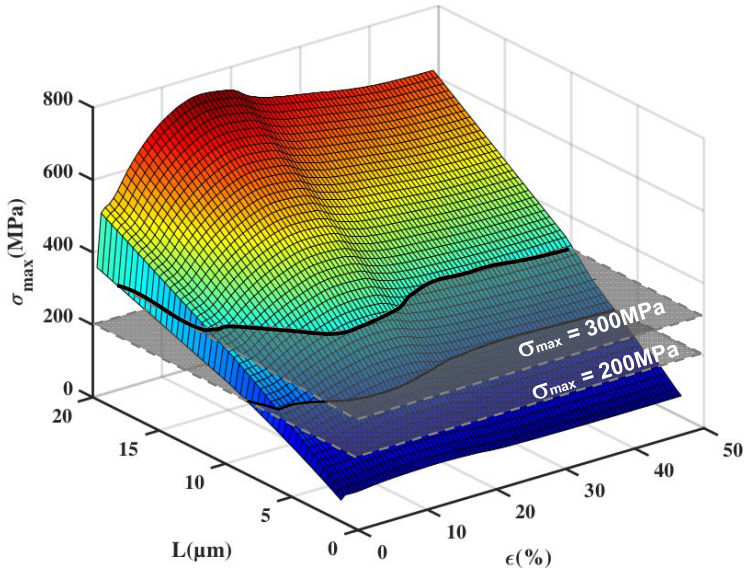

(a)

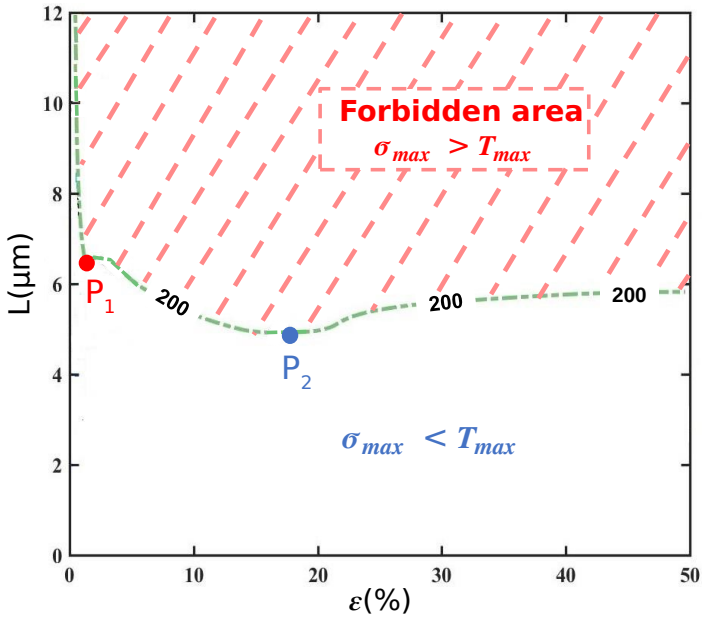

(b)

FIGURE 12: a) Isovalues of $\sigma_{max}(L, \bar{\epsilon})$ b) The example of a layer of strength $T_{max} = 200\ MPa$ is given, with 2 remarkable points P_1 and P_2 driving the saturation distances between approximately $2.5\mu m$ and $5\mu m$ depending on the initial island size L_0

This method can be repeated for any value of T_{max} allowing to predict the evolution of the minimum and maximum (blue dots respectively on Fig. 13(a) and (b))island lengths at saturation as a function of T_{max} . Both lengths evolve linearly with T_{max} and the zone in between the two curves corresponds to the predicted range of distance between consecutive cracks at saturation. Some of those ranges of distances between cracks at saturation are reported on Fig. 8 (see vertical dashed lines) for values of T_{max} which correspond to the one tested on large cell simulations. They clearly indicate an increase of the distance at saturation with T_{max} and it is worth noting that the range of distances at saturation is widening for increasing values of T_{max}. The results of the periodic unit cell compare quite well with the results of the large cell, confirming the previously observed trends. We thus show that both numerical methods allow the prediction of crack spacing at saturation with very similar accuracy but with a huge difference in term of calculation time of the same order of magnitude as the reduction of the cell's length.

The values of L_{max} obtained from our model have been compared with the data from two analytical models : from Hu and Evans [21] and Agrawal and Raj [24]. These models offer a simplified description of the mechanics of the problem, known as the shear lag approximation. These models assume that the material near the interface either yields or slides, while the rest of the substrate remains elastic. Thus it does not account for plastic deformation inside the bulk of the substrate, neither does it account for hardening. In contrast, our model includes these features.
The two shear lag models from [21] and [24] lead to a similar expression for the estimation of the distance between cracks at saturation :

$$\alpha \frac{\sigma_f}{\sigma_y} \leq \frac{L_{max}}{h} \leq 2\alpha \frac{\sigma_f}{\sigma_y} \tag{3}$$

with a constant α such that $\alpha = \sqrt{3}$ for [21] and $\alpha = \sqrt{3}\pi$ for [24], σ_y the yield stress , σ_f the tensile strength of the film and h the film thickness. The predictions of [21], [24] and our calculations have been ploted in Fig. 13. For the two shear lag models, the value $\sigma_y = 25$ MPa have been taken, which correspond to the quasi-plateau of our constitutive law (see Fig. 1). Remarkably, both our lower bound and upper bound predictions lies in between the values predicted by the two other approaches. Hence it seems that using one of the two shear lag models would tend to underestimate, or on the contrary overestimate the distance between cracks at saturation.

One main difference is that our study features a ceramic layer on top of a polymer substrate, whereas [21] and [24] describe ceramic layers on metal substrates. In our case, the film/substrate Young's moduli ratio is around 100 whereas it is less than 10 for ceramic/metal system. Also, the yield strain of our ETFE substrate (2%) is about 10 times higher than the yield strains of metallic substrates. These two features promote a large scale deformation of the substrate, well beneath the film/substrate interface, with shear bands extending far away inside the substrate, greatly influencing the redistribution of stresses in the system, and hence the distances between cracks at saturation. So, whereas shear lag models are justified in the case of metal/ceramic interfaces, they have to be used with caution in ceramic/polymers systems. As an particular illustration of this difference, it is worth noting that the extension of the plastic area within the substrate starting from each crack and spreading along the interface, (denoted a in Fig. 11), is seen to quickly saturate in our calculations (around an applied strain of $\epsilon = 1\%$). This shows that interface slip is indeed not what is controlling the saturation in the present case.

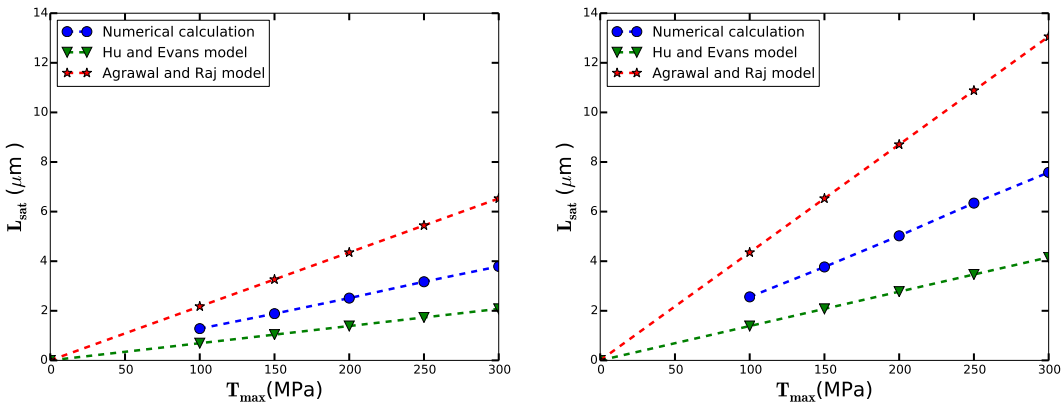

FIGURE 13: Comparison between values of L_{max} obtained from our calculation with data given by the models of Hu and Evans [21] and Agrawal and Raj [24] (a) lower bound, (b) upper bound.

3.2.3. Comparison between simulation and experimental results

Both simulation strategies used in this paper allow confirming our experimental hypothesis that plasticity in the substrate plays a major role in the selection of the length-scale at which saturation of fragmentation occurs. Indeed, simulation shows that plasticity starts to develop in the groove created by the presence of a crack in the film as it was observed in experiments. But, they also show that, plasticity does not remain confined at the interface between the film and the substrate but that it developed in the bulk at an angle close to 45°. The fact that two plastic regions initiated by two adjacent crack can merge in the bulk may be the main explanation for saturation length-scale. Indeed, in such situation, the connected plastic region act like a shield that prevents any further loading for the isolated film island. All the strain goes into the substrate and the film loading is even reduced which prevent any new cracks to appear.

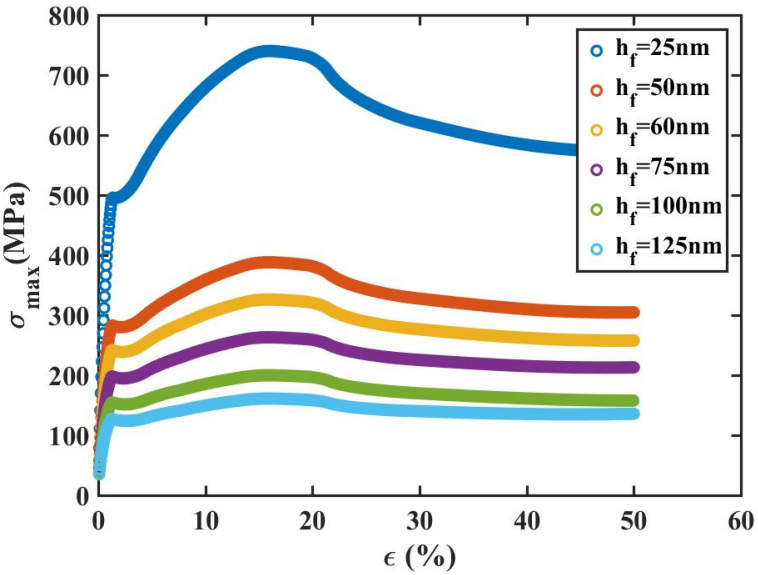

FIGURE 14: Evolution of σ_{max} versus nominal strain loading ϵ for $5\mu m$ unit cells simulation with different film thicknesses. σ_{max} is increasing for decreasing values of h_f.

As unit cell simulations are much efficient in term of computation time, we have been able to simulate a lot of realistic configuration to compare with experimental observations. We have perform simulation on $5\mu m$ size unit cells with different film thicknesses and plotted the evolution of σ_{max}

versus nominal strain loading ϵ on fig. 14. We show that σ_{max} is increasing for decreasing values of h_f . As higher σ_{max} leads to smaller inter-crack distance at saturation, we confirm the experimental observation that thicker layers also lead to larger fragments, for a given strain level (see Fig. 2b. If we assume a value for T_{max} of $200MPa$, we see on fig. 14 that all the two curves with $h_f > 100\mu m$ have a σ_{max} smaller than this value. Indeed, as the cell length is $5\mu m$, we can deduce that the saturation length for films close to $100nm$ thickness is of the order of $5\mu m$ which again corresponds very well to the experimental observations.

4. Conclusion

In this paper, multi-cracking of ZnO layers on ETFE under uniaxial traction has been investigated both by experimental and numerical approaches. We show the existence of three successive stages : random cracks, mid-island breaking and saturation of the crack pattern. The saturation regime at high strain leads to typical fragment sizes 50 times larger that the thickness of the layer that, in our opinion, origin from the emergence of localized plasticity in the substrate.

As classical models in literature does not allow to predict such experimental observations, a model accounting for large deformation and plasticity of a compliant substrates has been used to study brittle failure in the oxide thin layer and interface delamination. The use of cohesive zone models coupled to a statistical approach to simulate crack nucleation and propagations allowed for the observation of the 3 stages observed experimentally. Plasticity developing inside the substrate in the cracks areas proved to be a key phenomenon affecting both the range of interaction between two neighboring cracks and the value of the maximum stress reached right in between them. The weak hardening of ETFE is responsible for the saturation of this maximum stress value. The mid-cracks maximum stress value being saturated, any value of the layer strength T_{max} above this value causes saturation of the cracks pattern.

The subtle interplay between substrate plasticity and layer cracking has been captured by numerical simulations. The ranges of distances between cracks at saturation has been computed as a function of T_{max}, with two different numerical strategies, giving consistent results that are highly correlated with experimental observations. Finally it is worth noting that in the specific case of ETFE, with low hardening and very high ductility, the main

dissipation mechanism interplaying with layer cracking was clearly identified as plasticity in the substrate. It would be worth exploring other systems, as ZnO/PET, where more consequent interface delamination and even fracture in the substrate could occur as well.

Appendix

Description of the constitutive law for the cohesive zone model

The separation vector $\overrightarrow{\delta}$ and traction vector $\overrightarrow{T}$ can be resolved into their normal components (δ_n, T_n) which are related to the opening or mode I contribution and into their tangential components resolved in the direction normal to the crack front (δ_t, T_t) which are related to the shearing or mode II contribution. The law is a linear/softening model described in Fig. 15. In Stage 1, before reaching the peak traction, the traction-separation relation is linear and reversible with stiffness K :

$$\overrightarrow{T} = K\overrightarrow{\delta} \tag{4}$$

For any combination of traction components, (T_n, T_t), peak values $({T_n}^i, {T_t}^i)$ are reached when :

$$\left(\frac{T_n^i}{{T_n}^{max}}\right)^2 + \left(\frac{T_t^i}{{T_t}^{max}}\right)^2 = 1 \tag{5}$$

where T_n^{max} is the maximum traction in mode I and T_t^{max} is the maximum traction in mode II. The corresponding separations at the peak are $\overrightarrow{\delta^i} = (\delta_n^i, \delta_t^i)$ and $\overrightarrow{T^i} = (T_n^i, T_t^i)$

Once peak traction is attained (Stage 2), softening starts, resulting in decreasing traction. The separation energy/area G_c, which corresponds to the area under the curve in Fig. 15, is taken here to be independent of the mode mixity (mode II to mode I ratio).

A scalar effective relative interface displacement at complete separation, δ^f is defined from the relation [4] :

$$G_c = \frac{1}{2}\delta^f T^i \tag{6}$$

4. The two components δ_n^f and δ_t^f are determined using $G_c = \frac{1}{2}\delta_n^f T_n^i + \frac{1}{2}\delta_t^f T_t^i$.

where $T^i = \sqrt{T_n^{i\,2} + T_t^{i\,2}}$ is the peak stress magnitude.

The softening is implemented as a reduction of the stiffness by the factor $(1-D)$ where D can be regarded as a damage variable. The definition of the cohesive traction (i.e. Eq. 4) becomes :

$$\overrightarrow{T} = K(1-D)\overrightarrow{\delta} \tag{7}$$

The variable D is defined as

$$D = \frac{\delta^f}{\delta}\frac{\delta - \delta^i}{\delta^f - \delta^i} \tag{8}$$

where δ is the separation magnitude

$$\delta = \sqrt{\delta_n^2 + \delta_t^2} \tag{9}$$

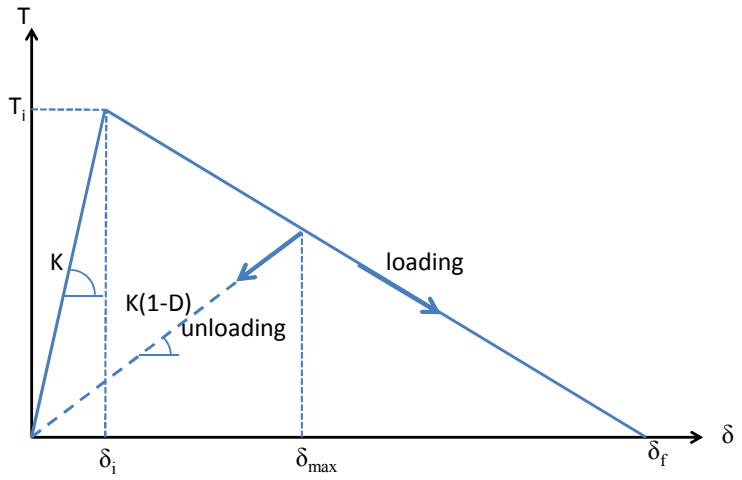

FIGURE 15: Linear softening traction vs separation law for the cohesive zone, with T_i the peak traction magnitude and δ^f the magnitude of the maximum opening at complete separation. The area underneath the curve is the toughness G_c.

Acknowledgements

This work was funded by the French National Research Agency program 'CAPRICE' (ANR-14-CE07-0024-03) and pertains to the French Govern-

ment program ‘Investissementsd’Avenir’ (LABEX INTERACTIFS, ANR-11-LABX-0017-01).

References

[1] J.W. Hutchinson and Z. Suo. Mixed mode cracking in layered materials. Advances in Applied Mechanics, 29 :63–191, 1992.

[2] Matthew R Begley and John W Hutchinson. The Mechanics and Reliability of Films, Multilayers and Coatings. Cambridge University Press, 2017.

[3] H. Jiang, D.-Y. Khang, J. Song, Y. Sun, Y. Huang, and J.A. Rogers. Finite deformation mechanics in buckled thin films on compliant supports. Proceedings of the National Academy of Sciences, 104(40) :15607–15612, 2007.

[4] J.A. Rogers, T. Someya, and Y. Huang. Materials and mechanics for stretchable electronics. Science, 327(5973) :1603–1607, 2010.

[5] D.-H. Kim et al. Epidermal electronics. Science, 333(6044) :838–843, 2011.

[6] Jay S Lewis and Michael S Weaver. Thin-film permeation-barrier technology for flexible organic light-emitting devices. IEEE Journal of selected topics in quantum electronics, 10(1) :45–57, 2004.

[7] N. Bowden, S. Brittain, A.G. Evans, J.W. Hutchinson, and G.M. Whitesides. Spontaneous formation of ordered structures in thin films of metals supported on an elastomeric polymer. Nature, 393(6681) :146–149, 1998.

[8] H. Mei, R. Huang, J.Y. Chung, C.M. Stafford, and H.H. Yu. Buckling modes of elastic thin films on elastic substrates. Applied Physics Letters, 90(15) :151902, 2007.

[9] A. Takei, L. Jin, J.W. Hutchinson, and H. Fujita. Ridge localizations and networks in thin films compressed by the incremental release of a large equi-biaxial pre-stretch in the substrate. Advanced Materials, 26(24) :4061–4067, 2014.

[10] G. Gille and B. Rau. Buckling instability and adhesion of carbon layers. Thin Solid Films, 120 :109–121, 1984.

[11] M.W. Moon, H.M. Jensen, J.W. Hutchinson, K.H. Oh, and A.G. Evans. The characterization of telephone cord buckling of compressed thin films on substrates. Journal of the Mechanics and Physics of Solids, 50(11) :2355–2377, 2002.

[12] D. Vella, J. Bico, A. Boudaoud, B. Roman, and P.M. Reis. The macroscopic delamination of thin films from elastic substrates. Proceedings of the National Academy of Sciences, 106(27) :10901–10906, 2009.

[13] J.-Y. Faou, G. Parry, S. Grachev, and E. Barthel. Telephone cord buckles a relation between wavelength and adhesion. Journal of the Mechanics and Physics of Solids, 75 :93 – 103, 2015.

[14] J.L. Beuth. Cracking of thin bonded flms in residual tension. Int. J. Solids Structures, 29 :1657–1675, 1992.

[15] Y Leterrier, L Boogh, J Andersons, and J-AE Månson. Adhesion of silicon oxide layers on poly (ethylene terephthalate). i : Effect of substrate properties on coating's fragmentation process. Journal of Polymer Science Part B : Polymer Physics, 35(9) :1449–1461, 1997.

[16] S. Frank, P.A. Gruber, U.A. Handge, and R. Spolenak. In situ studies on the cohesive properties of α and $\beta-$ ta layers on polyimide substrates. Acta Materialia, 59(15) :5881–5892, 2011.

[17] M.D. Thouless, Z. Li, N.J. Douville, and S. Takayama. Periodic cracking of films supported on compliant substrates. Journal of the Mechanics and Physics of Solids, 59(9) :1927–1937, 2011.

[18] S. Yang, B. Su, G. Bitar, and N. Lu. Stretchability of indium tin oxide (ito) serpentine thin films supported by kapton substrates. International Journal of Fracture, 190(1) :99–110, 2014.

[19] N. Lu, X. Wang, Z. Suo, and J. Vlassak. Metal films on polymer substrates stretched beyond 50%. Applied Physics Letters, 91(22) :221909, 2007.

[20] Nicholas J Douville, Zhengyu Li, Shuichi Takayama, and MD Thouless. Fracture of metal coated elastomers. Soft Matter, 7(14) :6493–6500, 2011.

[21] MS Hu and AG Evans. The cracking and decohesion of thin films on ductile substrates. Acta Metallurgica, 37(3) :917–925, 1989.

[22] MM Nagl, SRJ Saunders, WT Evans, and DJ Hall. The tensile failure of nickel oxide scales at ambient and at growth temperature. Corrosion Science, 35(5-8) :965971–969977, 1993.

[23] Z Cedric Xia and John W Hutchinson. Crack patterns in thin films. Journal of the Mechanics and Physics of Solids, 48(6) :1107–1131, 2000.

[24] Dinesh C Agrawal and R Raj. Measurement of the ultimate shear strength of a metal-ceramic interface. Acta Metallurgica, 37(4) :1265–1270, 1989.

[25] Y. Leterrier, J. Andersons, Y. Pitton, and J.A. Månson. Adhesion of silicon oxide layers on poly (ethylene terephthalate). ii : Effect of coating thickness on adhesive and cohesive strengths. Journal of Polymer Science Part B : Polymer Physics, 35(9) :1463–1472, 1997.

[26] Yves Leterrier. Durability of nanosized oxygen-barrier coatings on polymers. Progress in Materials Science, 48(1) :1–55, 2003.

[27] MJ Cordill, A Taylor, J Schalko, and G Dehm. Fracture and delamination of chromium thin films on polymer substrates. Metallurgical and Materials Transactions A, 41(4) :870–875, 2010.

[28] S. Frank, U.A. Handge, S. Olliges, and R. Spolenak. The relationship between thin film fragmentation and buckle formation : Synchrotron-based in situ studies and two-dimensional stress analysis. Acta Materialia, 57 :1442–1453, 209.

[29] H. M. Jensen, J. W. Hutchinson, and K. Kyung-Suk. Decohesion of a cut prestressed film on a substrate. International Journal of Solids and Structures, 26(9-10) :1099–114, 1990.

[30] A.A.L. Baldelli, B. Bourdin, J.J. Marigo, and C. Maurini. Fracture and debonding of a thin film on a stiff substrate : analytical and numerical solutions of a one-dimensional variational model. Continuum Mechanics and Thermodynamics, pages 1–26, 2013.

[31] MJ Cordill and AA Taylor. Thickness effect on the fracture and delamination of titanium films. Thin Solid Films, 589 :209–214, 2015.

[32] Z Suo. Reliability of interconnect structures. Volume, 8 :265–324, 2003.

[33] X.P. Xu and A. Needleman. Void nucleation by inclusion debonding in a crystal matrix. Model. Simul. Mater. Sci. Eng., 1 :111–132, 1993.

[34] V. Tvergaard and J. W. Hutchinson. The relation between crack growth resistance and fracture process parameters in elastic-plastic solids. J. Mech. Phys. Solids, 40 :1377–1397, 1992.

[35] Dassault Systèmes Simulia Corp., Providence, RI, USA. ABAQUS Manuals Collection, 2013.

[36] A. Needleman. A continuum model for void nucleation by inclusion debonding. Journal of Applied Mechanics, 54 :525–531, 1987.

[37] L. B. Freund and Y. Hu. Shear stress at a film-substrate interface due to mismatch strain. Technical report, Brown Univ Providence RI Div of Engineering, 1988.